Materials Science & Engineering A xxx (xxxx) 142179

Contents lists available at ScienceDirect

Materials Science & Engineering A

journal homepage: www.elsevier.com/locate/msea

In-situ formation of TiC nanoparticles in selective laser melting of 316L with addition of micronsized TiC particles

Wengang Zhai [a], Wei Zhou [a,*], Sharon Mui Ling Nai [b,**]

[a] School of Mechanical and Aerospace Engineering, Nanyang Technological University, 50 Nanyang Avenue, 639798, Singapore
[b] Singapore Institute of Manufacturing Technology, 73 Nanyang Drive, 637662, Singapore

ARTICLE INFO

Keywords:
Additive manufacturing
Metal matrix composite
Grain refinement
Stainless steel
TiC particles
Orowan strengthening

ABSTRACT

316L stainless steel has a wide range of engineering applications. However, its relatively low yield strength limits its applications. In this work, strengthened 316L stainless steel was fabricated via selective laser melting (SLM) with the addition of 3 wt% micronsized TiC particles. The grains of 316L are significantly refined to approximately 3 μm. Although micronsized TiC particles were used as reinforcement, in-situ formed nanosized TiC particles were observed. Tensile tests were carried out and the yield strength of SLM 316L-3TiC was 803 MPa–832 MPa with the elongation ranging from 25.8% to 28.5% when fabricated with laser power between 225 W and 275 W. Relative to SLM 316L without TiC particles which has a yield strength of 599 MPa, the strength enhancement is found to be 97 MPa from grain refinement and 140 MPa from Orowan strengthening.

1. Introduction

Developing lightweight and cost-efficient alloys with superior mechanical properties is attractive for a variety of structural applications. Among the various alloys, austenitic stainless steels are widely used in engineering applications due to their excellent corrosion and oxidation resistance. Among the numerous types of austenitic stainless steels, 316L has a wide range of engineering applications and therefore provides the impetus for widespread processing-structure-property based studies. However, its relatively low yield strength (170 MPa, according to ASTM A240) hinders its wider applications. There has been a growing interest in developing 316L with high strength and good ductility [1–3].

Currently, the main method used in enhancing the mechanical properties of 316L is grain refinement, which can be achieved through annealing following severe plastic deformation by cold rolling [4], equal channel angular pressing [5], high-pressure torsion [6] or dynamic plastic deformation with high strain rate [2]. During severe plastic deformation, a large amount of strain-induced martensite is produced. Following this, the needle-like martensite can be reverted to nano-/ultrafine-grained austenitic structure by thermal annealing. These ultrafine grains can result in an enhancement of strength [3,7,8] with a simultaneous increase in ductility. However, the severe plastic deformation processes are often too complex to be incorporated into industrial production.

Recently, additive manufacturing has gained tremendous attention owing to its great advantage in fabricating components with complex geometry using a layer-wise building method which allows the customization of production of engineering parts with desired configurations. Importantly, additive manufacturing is a high throughput and energy efficient process. Selective laser melting (SLM) is a specific type of additive manufacturing technique which utilizes high power-density laser to melt powders. Compared to conventional wrought 316L, higher yield strength of up to 600 MPa has been reported for SLM fabricated 316L, without compromising ductility [1,9–12].

The introduction of foreign reinforcements is a potent strategy to further improve the yield strength of SLM fabricated 316L metal matrix composites (MMCs). The small melting zone (~100 μm in width and depth) and fast cooling rate (10^6 - 10^8 K/s) helps to prevent the particles from segregation. The coarsening of reinforcements can also be prevented due to the fast cooling rate (10^6 - 10^8 K/s) of SLM [13,14]. These are advantages of SLM in terms of fabricating MMCs when compared to traditional methods, such as casting and powder metallurgy which would lead to undesirable coarse grains and inhomogeneous distribution of reinforcements.

Among the various types of particulate reinforcements, TiC is commonly used to strengthen Fe-based alloys due to its low density, supe-

* Corresponding author.
** Corresponding author.
E-mail addresses: wzhou@cantab.net; mwzhou@ntu.edu.sg (W. Zhou), mlnai@simtech.a-star.edu.sg (S.M.L. Nai).

https://doi.org/10.1016/j.msea.2021.142179
Received 7 July 2021; Received in revised form 3 October 2021; Accepted 9 October 2021
0921-5093/

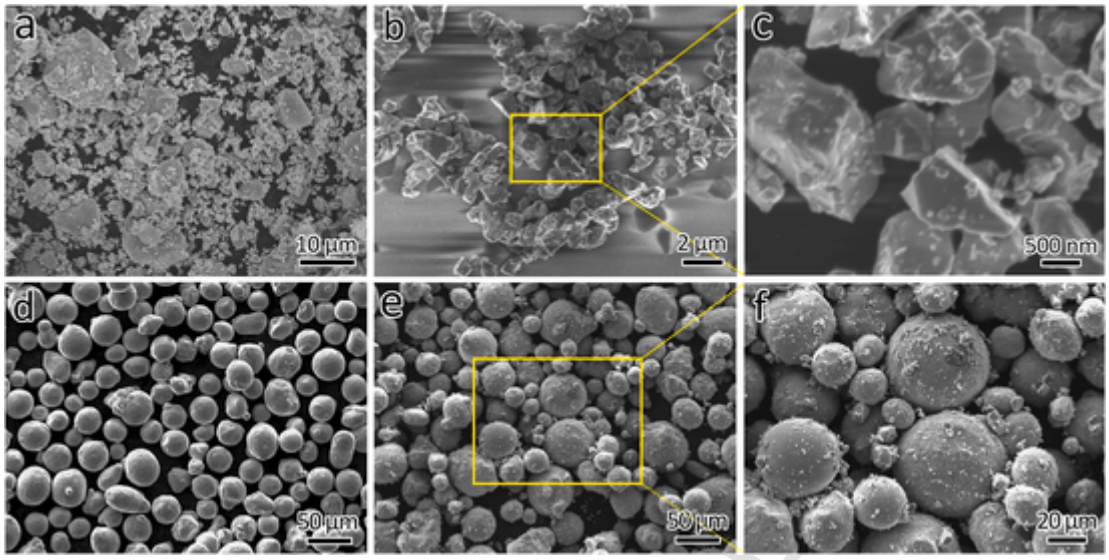

Fig. 1. (a) Micronsized TiC particles; (b) a larger number of particles of sizes 0.5–2 μm; (c) a close-up of the small TiC particles; (d) 316L powder; (e) 316L-3TiC powder mixture; and (f) a close-up of (e) showing the distribution of TiC particles.

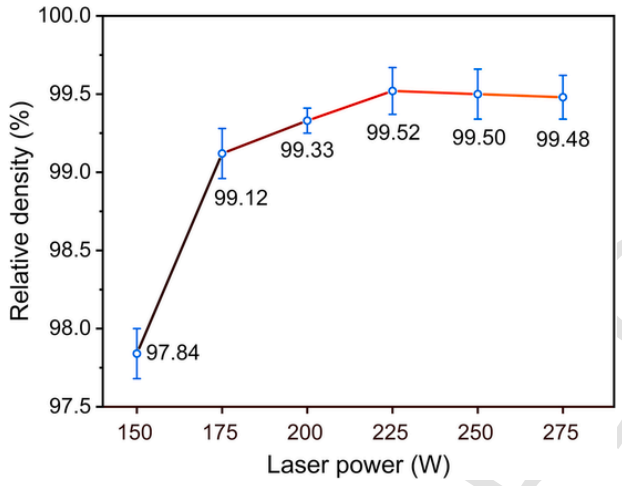

Fig. 2. Relative density of SLM 316L-3TiC fabricated with different laser powers.

rior corrosion resistance, high hardness, as well as thermodynamic and thermal stability in Fe-based alloys AlMangour et al. [15,16] have previously attempted SLM of TiC reinforced 316L. However, high energy ball milling was applied to prepare the powder feedstock in their work. It is well known that efficiency can be a problem when the high energy ball milling process is applied. After the high energy ball milling process, the shape of 316L powder becomes irregular. For SLM, the spherical powder is preferred because of its good flowability. Moreover, they obtained the yield strength from compression tests, which are less sensitive to defects (such as porosity and lack of fusion) than tensile tests. It has been reported that fracture strain measured from compressive test is larger than that from tensile test for SLM MMCs with defects [17]. Therefore, it is not known whether the strengthening of TiC particles to 316L is gained at the expense of drastically reduced ductility. In another instance, Zhao et al. [18] studied the SLM of 316L with nano-TiC reinforcement. The powder feedstock was prepared by direct mixing. After the mixing, the nanosized TiC particles were uniformly distributed on the surface of the 316L power. Unfortunately, the highest ultimate tensile strength of nano-TiC-reinforced 316L was measured at only 748.6 MPa, which was even lower than SLM 316L without any reinforcement. The reason may lie in the choice of laser processing parameters, which could have resulted in the low relatively density (96%–99%) of the materials they prepared. Therefore, further studies need to be conducted on TiC particles strengthened 316L using SLM.

In our previous work [19], it was demonstrated that the addition of 1 wt% and 3 wt% micronsized TiC particles led to a significant increase in yield strength (660 MPa and 832 MPa) while maintaining good ductility (56% and 29% elongation). The strength enhancement is attributed to the grain refinement as well as the dispersed TiC particles. However, the effect of laser power on the densification behavior, microstructure evolution and mechanical performance is still unclear. Moreover, with the addition of 3 wt% micronsized TiC particles, the yield strength was increased by 233 MPa (from 599 MPa to 832 MPa). The increase was attributed to grain refinement and Orowan strengthening. However, calculations performed using the Hall-Petch relationship [7] and the Ashby-Orowan relationship [20] showed that the enhancement was much less than the experimental result. Therefore, further research should be conducted to study the strengthening mechanisms. In this work, different laser powers were used for fabricating SLM 316L-3TiC. A detailed investigation has been carried out to evaluate the effect of laser power on densification behavior, microstructure evolution, mechanical performance and the strengthening mechanism.

2. Materials and methods

2.1. 316L powder and TiC particles

Commercial 316L powder (Höganäs, Belgium) with the chemical composition of Fe-16.8Cr-12.7Ni-2.5Mo-1.5Mn-0.7Si-0.011C-0.074O (wt%) was used for SLM. The mean size of the powder was measured as 42.3 μm using an LA-960 laser scattering particle size distribution analyzer. TiC particles, as shown in Fig. 1(a), with the size ranging from 0.5 to 21 μm were added as reinforcement. There is a large amount of small TiC particles of sizes 0.5–2 μm, as shown in Fig. 1(b and c). The morphology of 316L powder is shown in Fig. 1(d).

3 wt% of TiC particles were added to 316L powder. The 316L-3TiC powder mixture was prepared using a low energy ball milling process, which was described in our previous work [19]. Using this method, the TiC particles can be uniformly distributed on the surface of 316L powder, as shown in Fig. 1(e and f). The low energy ball milling method is efficient and only has a negligible effect on the shape and flowability of 316L powder [21]. It can be a potential method for the preparation of the powder feedstock of additively manufactured metal matrix composites.

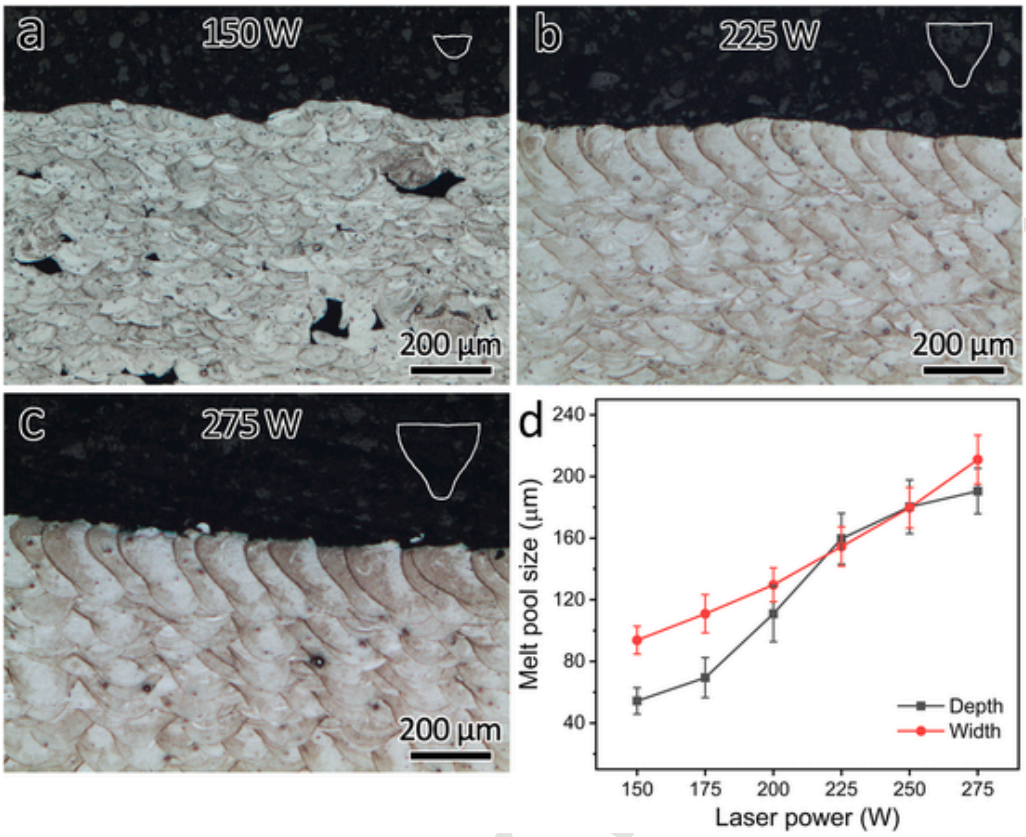

Fig. 3. Optical micrographs and drawings (insets) showing evolution of melt pool size and morphology with increasing laser power.

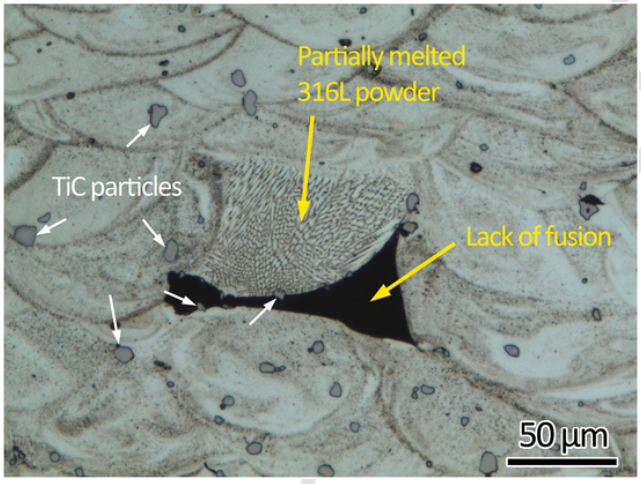

Fig. 4. Formation of cavity due to partial melting of 316L powder.

2.2. SLM facility and printing procedure

SLM was conducted using ProX DMP 300 (3D systems, South Carolina, US) equipped with a 500 W continuous wave fiber laser with a wavelength of 1.070 μm and beam diameter of 75 μm at the focal point. The printing chamber was filled with Ar gas to limit the oxygen content to below 300 ppm. The laser scanning direction was rotated 90° between two adjacent layers. To study the effect of laser power on the microstructure and mechanical properties of 316L-3TiC, different laser powers of 150, 175, 200, 225, 250 and 275 W were selected. The laser scanning speed was kept at 800 mm/s. The layer thickness was kept as 30 μm. The hatch spacing was kept as 70 μm.

2.3. Microstructure characterization

The microstructures were observed using optical microscope, Scanning Electron Microscope (SEM, JEOL 7600F), Energy Dispersive X-Ray Spectroscopy (EDS), X-Ray diffraction (XRD, PANalytical Empyrean), Electron Backscattered Diffraction (EBSD) and Transmission Electron Microscope (TEM, JEOL 2010). The samples for microstructural analyses were firstly ground with progressively finer SiC papers (320–4000 grit) and then polished with silicon oxide polishing suspension (OP–S). A self-mixed etching solution (HF: HNO_3: H_2O = 1: 6: 12) was used for cellular structure and melt pool observations under the optical microscope and SEM. The accelerating voltage of 10 kV was used for the SEM observation. XRD measurement was conducted using Cu $K_{\alpha 1}$ (λ = 0.15406 nm) at 30 kV and 30 mA with the step size of 0.01° and scan speed of 1.2°/min. A step size of 0.6 μm and accelerating voltage of 20 kV were used for EBSD observation. TEM sample was prepared using ion milling and the sample was observed at the accelerating voltage of 200 kV.

2.4. Mechanical properties

Microhardness and tensile tests were performed to investigate the mechanical properties of SLM 316L-3TiC fabricated with different laser powers. Microhardness was measured under 500 g with a dwell time of 15 s. For each sample, 21 indentations were tested. Tensile tests were conducted at room temperature at the strain rate of 10^{-3} s^{-1} using Instron 5982 universal tensile testing machine. The gauge dimensions of the tensile samples were 14 mm × 4 mm × 2 mm. A non-contact Instron AVE 2 extensometer was used to measure the tensile strain. Three tensile samples were tested for each condition.

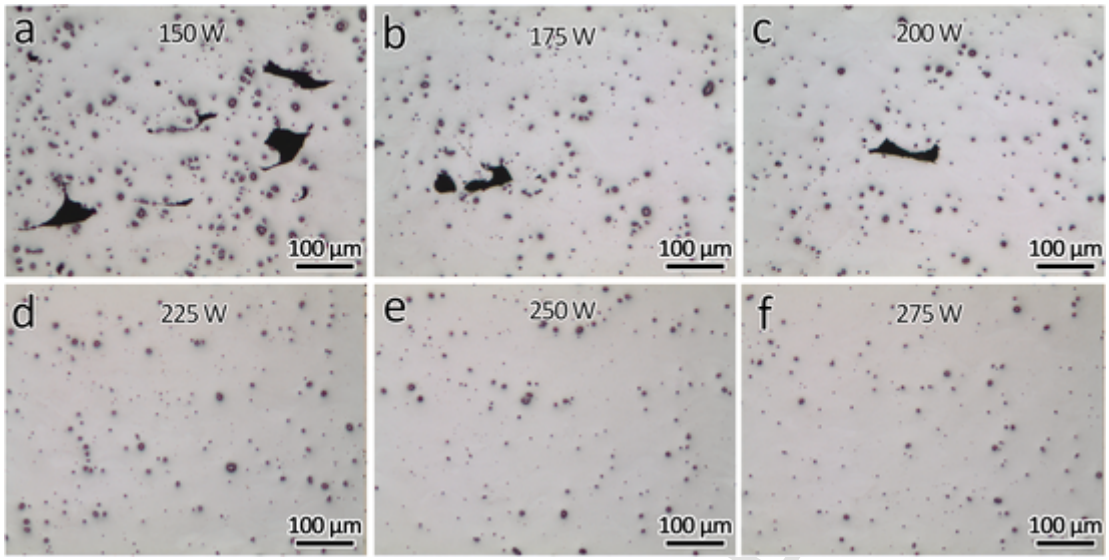

Fig. 5. Evolution of number and size of TiC particles with increasing laser power from 150 W to 275 W.

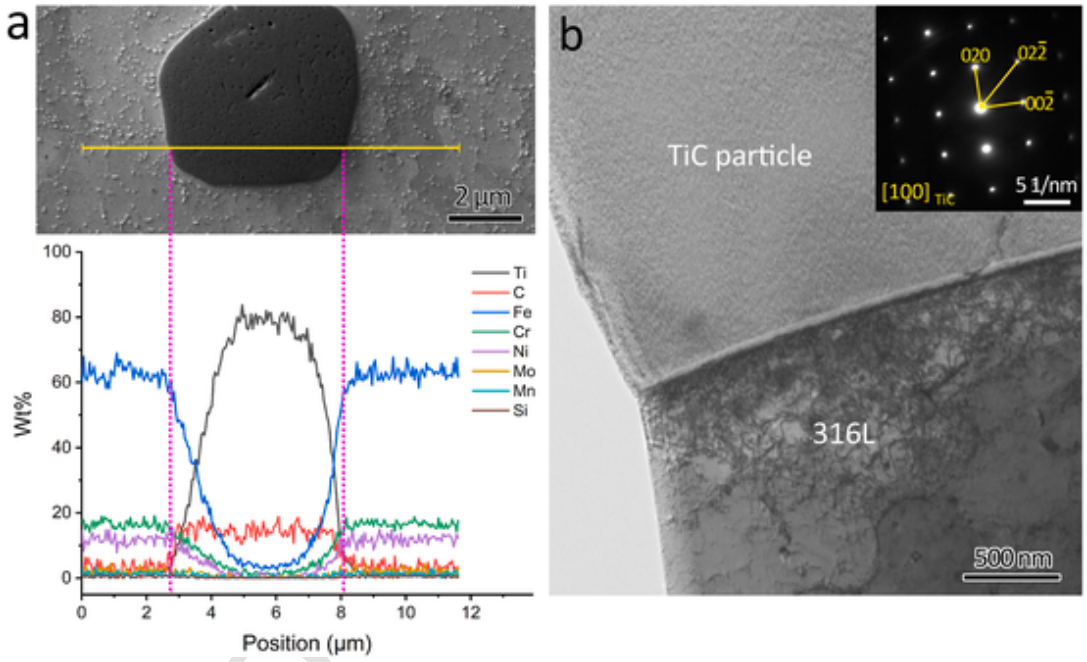

Fig. 6. (a) EDS line scan and (b) TEM bright-field image showing that there is no intermetallic layer between micronsized TiC particles and 316L matrix and their good bonding, with the embedded image in (b) showing the SAED pattern of a TiC particle.

3. Results

3.1. Densification behavior

Samples of dimensions 10 × 10 × 25 mm^3 were prepared for the density measurement. The density was measured based on Archimedes principle and the relative density was calculated, as shown in Fig. 2. At low laser power of 150 W, the relative density was only 97.84%. With the increase of laser power, the highest relative density (99.52%) was achieved at the laser power of 225 W. The relative density was slightly decreased with a further increase of laser power. Notably, the relative density of SLM 316L-3TiC fabricated with laser powers of 225, 250 and 275 W were all near 99.5% which was very close to full density.

To get near fully dense selective laser melted alloys, various parameters (laser power, laser scanning speed, layer thickness, hatch spacing, etc.) should be carefully optimized. The heat input for the melting of powders mainly depends on the laser power and scanning speed. During the SLM process, the melt pool depth should be larger than the layer thickness and overlapping of the adjacent laser tracks is necessary to avoid lack of fusion.

To reveal the relationship between relative density and laser power, the size of the melt pool was observed, as shown in Fig. 3. Owing to the unique track-by-track and layer-by-layer building strategy of the SLM process, the as-built SLM 316L-3TiC presented a hierarchical microstructure. The melt pools of SLM 316L-3TiC fabricated with low heat input (150, 175 and 200 W) presented a conduction mode while that with high heat input (225, 250 and 275 W) presented a keyhole mode, as illustrated in the top right-hand corner of each figure in Fig. 3. The width and depth of the melt pools resulting from the application of different laser powers were measured and are summarized in Fig. 3(d). It can be seen that both width and depth were increased with increasing laser power.

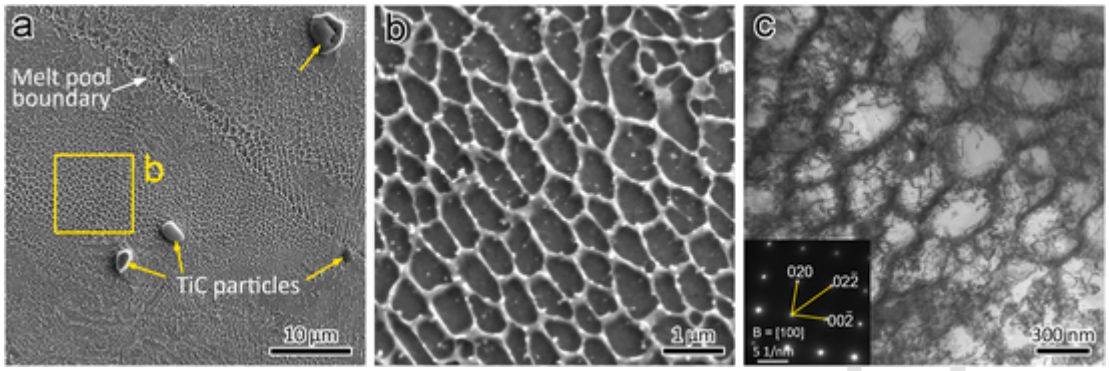

Fig. 7. (a) SEM image showing the overall microstructure of SLM 316L-3TiC using 225 W, (b) a close-up of the cellular structure and (c) TEM bright-field image showing the cellular structure boundaries consisting of dislocation networks, with the embedded image in (c) showing the SAED pattern of austenite phase.

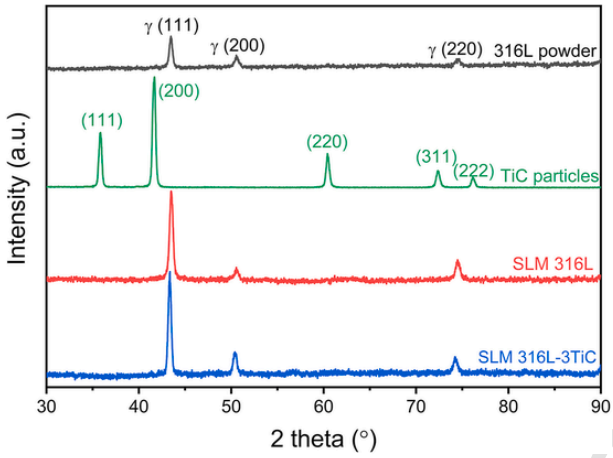

Fig. 8. XRD patterns of 316L powder, TiC particles, SLM 316L and 316L-3TiC.

Low heat input generated small melt pools which were not sufficient to fully melt the powder. In the SLM 316L-3TiC sample fabricated with laser power of 150 W, a partially melted 316L powder and a cavity were observed, as shown in Fig. 4. The cavity defect was the main reason for the low relative density of SLM 316L-3TiC fabricated with the laser power of 150 W. The irregular shape of the cavity gave rise to the sharp edges in the void. Sharp edges can act as crack initiation locations, which significantly impacted the mechanical properties of the final part.

at low laser power of 150 W.

3.2. Microstructure evolution of SLM 316L-3TiC

Fig. 5 shows the uniform distribution of the micronsized TiC particles in 316L matrix under different laser powers. No agglomeration of TiC particles was observed in the samples. With low heat input (150, 175 and 200 W), cavities were observed, as shown in Fig. 5(a, b and c). With the increase of laser power, near fully dense samples were obtained. Interestingly, as shown in Fig. 5, the size of TiC particles decreased with the increase of laser power. In particular, it can be seen clearly that the TiC particles are fewer in number and smaller in size in the 275 W sample than in the samples of lower powers of 150 W and 225 W. Furthermore, the TiC particles that are larger than 5 μm are counted as about 154, 64 and 40 in the samples of 150 W, 225 W and 275 W, as shown in Fig. 5(a, d and f). It can be deduced from the observation of the decreasing number and size of TiC particles with the increase of laser power that the micronsized TiC particles were partially melted and dissolved in the 316L melt during SLM. Notably, there were no cracks observed with the increase of laser power, indicating a big processing window for the fabrication of 316L-3TiC using SLM.

The EDS line scan in Fig. 6(a) shows that there was no intermetallic layer between TiC particles and 316L matrix, unlike TiC particles reinforced Inconel 718 [22] and WC reinforced 1.2767 L tool steel [23], which both contained an intermetallic layer between the particles and the matrix. As shown in Fig. 6(a and b), the micronsized TiC particles were observed to be well-bonded to the 316L matrix. The embedded image in Fig. 6(b) shows the selected area electron diffraction (SAED) pattern of a TiC particle with the zone axis of [001]. There were no gaps or cracks in the samples. The good bonding of the 316L matrix and the TiC particles can be attributed to the good wettability of these two materials at high temperatures. It has been reported that the contact angle of Fe-based austenitic steel and TiC ceramic was 30° at 1550 °C [24], indicating good wettability.

The overall etched microstructure of SLM 316L-3TiC using 225 W was observed to contain melt pool boundary, undissolved TiC particles and sub-micron subgrains, as shown in Fig. 7(a). These subgrains or cellular structures are frequently observed in SLM 316L without TiC addition [1,9,25]. Here a similar cellular structure was observed in the SLM microstructures with the addition of TiC particles. A close-up of the cellular structure observed using SEM is shown in Fig. 7(b). TEM observation shows that the cellular structure boundaries consisted of dislocation networks, as shown in Fig. 7(c), with an embedded image showing the SAED pattern of austenite phase. The high density dislocations are a result of repeated compression-tension cycles caused by the local thermal inhomogeneity during the SLM process [26]. The cellular structure boundaries consisted of the segregation of Cr and Mo elements [1], which was attributed to the constitutional undercooling during rapid solidification.

To examine the phase composition of TiC particles reinforced 316L, XRD measurement was conducted and the results are shown in Fig. 8. In 316L powder, only γ austenite phase was observed. After SLM process, the austenite phase was retained in SLM 316L. With the addition of 3 wt% TiC particles, only austenite phase was observed. No TiC phase was detected in 316L-3TiC because the content of TiC is low.

Fig. 9 presents the EBSD results of the SLM 316L-3TiC fabricated with different laser powers. During the EBSD measurement, the undetected area was controlled at lower than 1.8%. Standard zero solutions was performed using HKL channel 5 software. Only austenitic phase was detected, which means the phase composition of 316L remained unchanged with the addition of TiC particles.

Strong epitaxial growth tendency which leads to a highly anisotropic microstructure is frequently observed in SLM 316L [19,27]. No obvious epitaxial grains were observed in SLM 316L-3TiC samples fabricated with laser power of 175, 200, 225 or 250 W, as shown in Fig. 9(a–d). The only exception is the sample fabricated with the highest laser power of 275 W, in which elongated epitaxial grains can be detected, as shown in Fig. 9(e and f). Pole figures for the 225 W samples are shown in Fig. 9(g) and the maximum texture index is found to be low at 2.36. It is very close to the texture index of annealed wrought

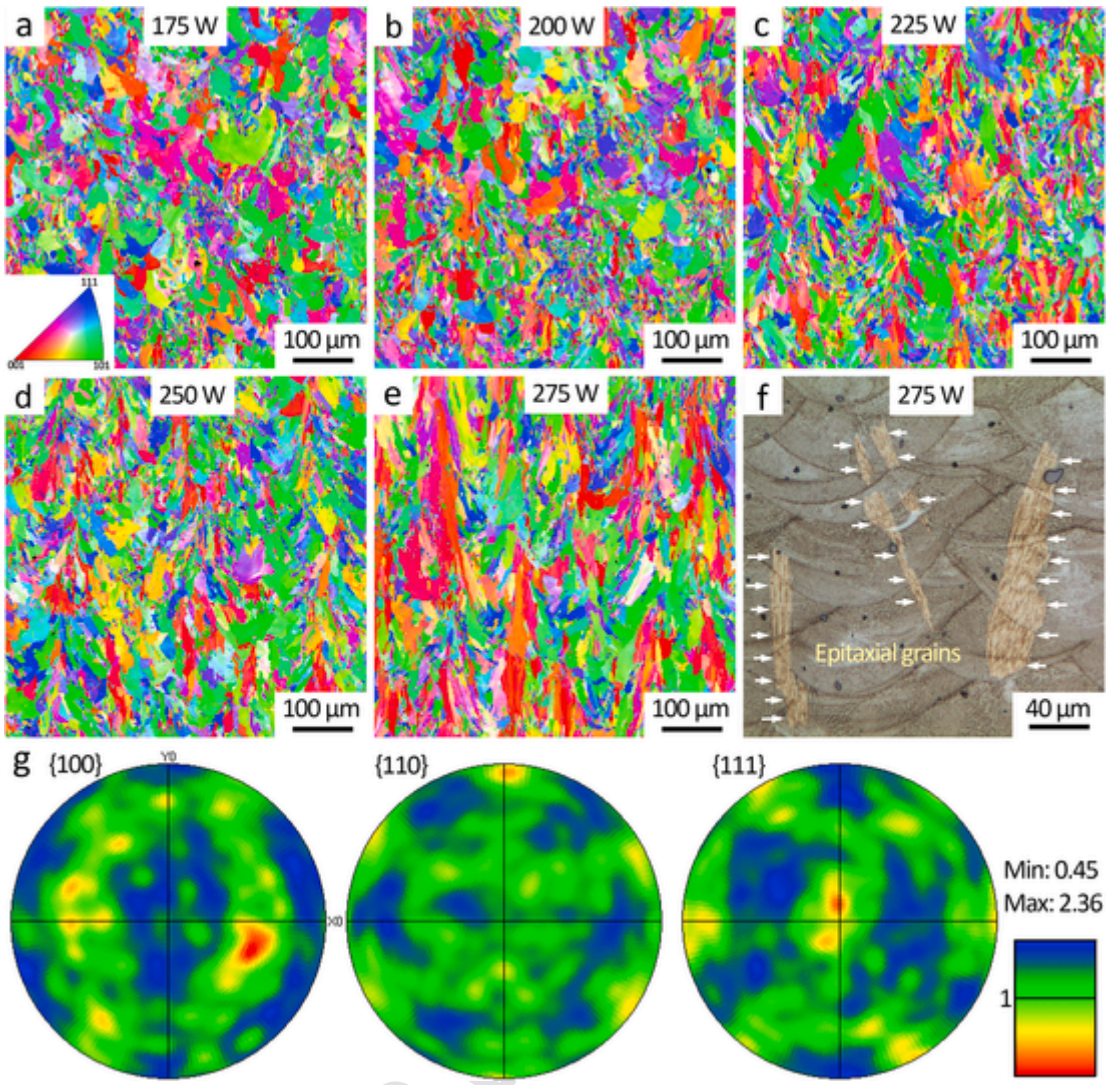

Fig. 9. (a) to (e) EBSD results showing morphology of grains and epitaxial growth with increasing laser power. (f) Optical micrograph showing clearly epitaxial grains (pointed) at the highest laser power of 275 W. (g) Pole figures derived from (c).

316L steel, which is 1.8 [28]. The texture index of an isotropic microstructure equals 1. 316L fabricated using SLM normally presents a strong anisotropic microstructure, and the texture index derived from pole figures can be as high as 11 [29]. However, SLM 316L-3TiC presented a much less anisotropic orientation with the texture index of 2.36, indicating that the addition of TiC particles can decrease the anisotropic tendency.

Epitaxial growth can occur during the SLM process of 316L leading to the evolution of a <001> texture, which was a result of the super large cooling rate (10^6 - 10^8 K/s) of SLM. During the solidification, the preceding layer serves as a seed. The grains in the newly printed layer grow epitaxially in the crystalline orientation consistent with that of the seed. Thus, elongated grains are frequently observed in selective laser melted cubic materials.

The addition of TiC particles catalyzes the nucleation event by increasing the number of heterogeneous nuclei in the melt, enabling austenitic grains to nucleate heterogeneously on the surface of TiC particles, leading to a refined microstructure. TiC particles are efficient for the grain refinement of stainless steels because of their small contact angle. The free energy barrier for heterogenous nucleation is affected by the contact angle of the melt and nucleus. The smaller contact angle would stimulate the heterogenous nucleation by reducing the volume of the critical nucleus. That is to say, the better the wettability, the more efficient the nucleation is.

The average grain size of SLM 316L-3TiC fabricated with different laser powers is summarized in Fig. 10, which was derived from the EBSD results in Fig. 9. It can be seen that the grains coarsened with the increase of laser power. The average grain sizes of SLM 316L-3TiC were 2.7, 2.9, 3.2, 3.3 and 3.5 μm when fabricated with laser powers of 175, 200, 225, 250 and 275 W, respectively. Two factors affected the grain size of SLM 316L-3TiC. One was the heat input that came from the laser. The other one was the heterogeneous nucleation contributed by the TiC particles. These two factors affected the grain size in a competitive mechanism. High heat input would lead to the coarsening of the grains and a simultaneous partial melting of the micronsized TiC particles, which introduces a large number of nanosized TiC particles that can act as heterogeneous nucleation sites. However, SLM 316L-3TiC fabricated with high laser power had a larger grain size which means the high heat input had an overall larger effect on the grain size although more in-situ TiC nanoparticles were formed. With laser power of 175 W, 24.3% of grains were smaller than 1 μm and 3.2% of grains were bigger than 10 μm. In comparison, 21. 3%, 20.7%, 20.3% grains were smaller than 1 μm and 3.8%, 5.0% and 5.4% grains were larger than 10 μm with the laser power of 200, 225, and 250 W. The higher

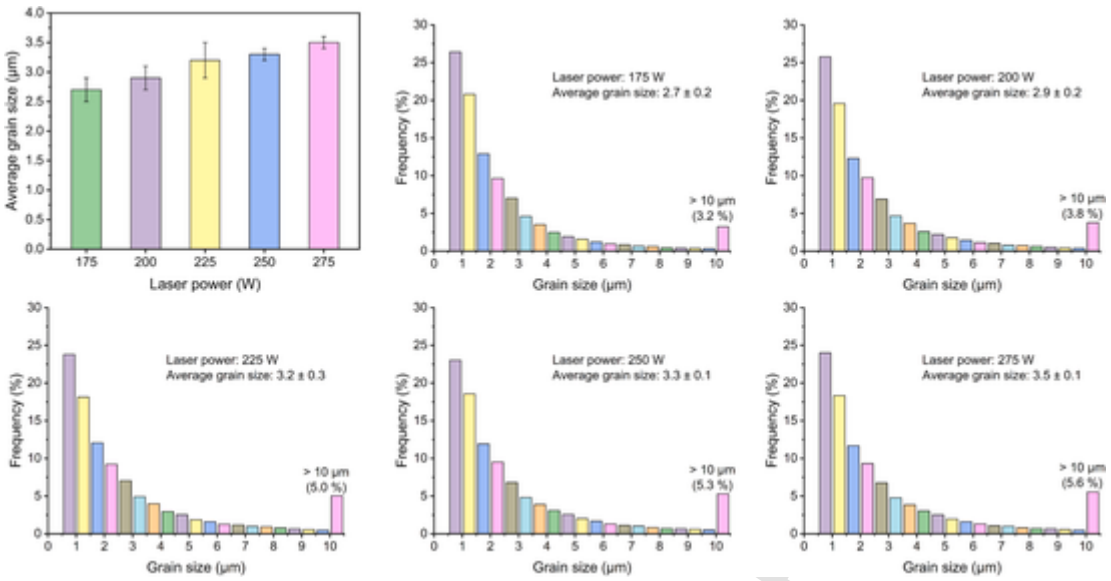

Fig. 10. Effect of laser power on average grain size and grain size distribution.

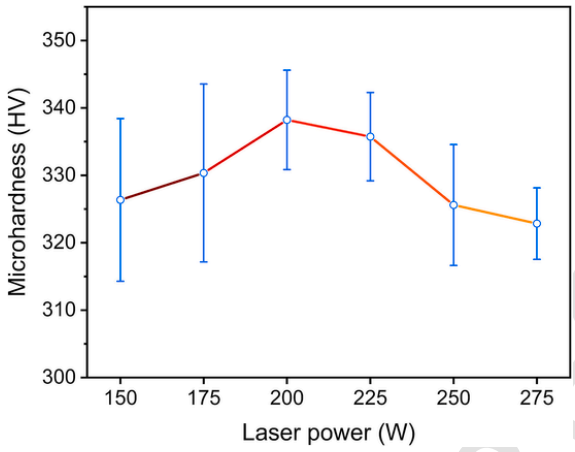

Fig. 11. Effect of laser power on microhardness.

heat input decreased the quantity of the small grains and increased that of the large grains.

3.3. Mechanical properties of SLM 316L-3TiC

The microhardness of SLM 316L-3TiC is shown in Fig. 11. Typically, metallic materials would have a higher microhardness if the average grain size is smaller. However, the microhardness of SLM 316L-3TiC fabricated with the laser power of 150 W and 175 W (which had a smaller grain size) was lower than that of 200 W (which had a larger grain size). This can be attributed to the larger number of TiC nanoparticles in the 200 W sample. With the near fully dense samples (200, 225, 250, and 275 W), the microhardness was slightly decreased with the increase of laser power, due to the larger average grain size as measured using the EBSD results. The sample fabricated with the laser power of 200 W had the highest microhardness of 338.2 HV. Overall, the microhardness of SLM 316L-3TiC is increased significantly, compared with the microhardness of SLM pure 316L which is about 240 HV.

The tensile stress-strain curves of SLM 316L-3TiC fabricated with different laser powers are presented in Fig. 12(a–e). The results are summarized in Fig. 12(f). It can be seen that the elongation of SLM 316L-3TiC fabricated with laser powers of 175 W and 200 W were very low at 10.3% and 10.6% respectively. The low elongation is attributed to the high content of cavities in the samples. The fractographs presented in Fig. 13 show the cavities in the sample fabricated with laser power of 175 W. Unmelt powders (Fig. 13(b)) and a cavity (Fig. 13(c)) were observed in the sample. The sharp corners of the cavity caused premature fracture during tensile test, because fracture is highly sensitive to defects [30]. Besides the elongation, the yield strength (σ_y) and ultimate tensile strength (UTS) of samples prepared with laser powers of 175 W and 200 W were also lower than that of higher laser powers. Defects are the main reasons for the low elongation and low strength in the samples prepared with laser powers of 175 W and 200 W. In additively manufactured samples, a cavity has a fatal effect on elongation and strength and thus should be avoided.

The samples fabricated with the laser power of 225 W showed the highest yield strength (832 MPa), UTS (1032 MPa) and elongation (28.5%). The yield strength of SLM 316L-3TiC fabricated with laser powers of 250 W and 275 W was 821 MPa and 803 MPa, respectively. As laser power increased from 250W to 275W, there was a decrease in the yield strength because of the larger grains resulting from higher heat input. The elongation of SLM 316L-3TiC fabricated with laser powers of 250 W and 275 W was 25.8% and 28.2%, respectively. The relatively high elongation is because of the high density of the samples. No cavity was observed in the fractured samples fabricated with the laser power of 225 W, 250 W and 275 W, as shown in Fig. 14. The TiC particles were found to be cracked. This is not surprising since ceramic particles are known to be brittle in nature. Importantly, the cracked TiC particles demonstrated that the TiC particles were well-bonded to the matrix. If the interface between TiC and 316L matrix were weak, the particles could have been debonded from the matrix rather than cracked. This conclusion is consistent with the observation of polished and unetched samples presented earlier (Fig. 6(a)). Dimples can be seen on the fracture surface, indicating ductile fracture mode.

4. Discussion

4.1. In-situ formation of TiC nanoparticles

Uniformly distributed TiC nanoparticles were observed using SEM under the accelerating voltage of 10 kV from a non-etched 316L-3TiC sample fabricated using 225 W, as shown in Fig. 15(a). This phenomenon was observed in all the samples fabricated using different laser powers. Although a large number of small particles of sizes ranging from 0.5 to 2 μm is present in the raw TiC particles (Fig. 2(b)), they are

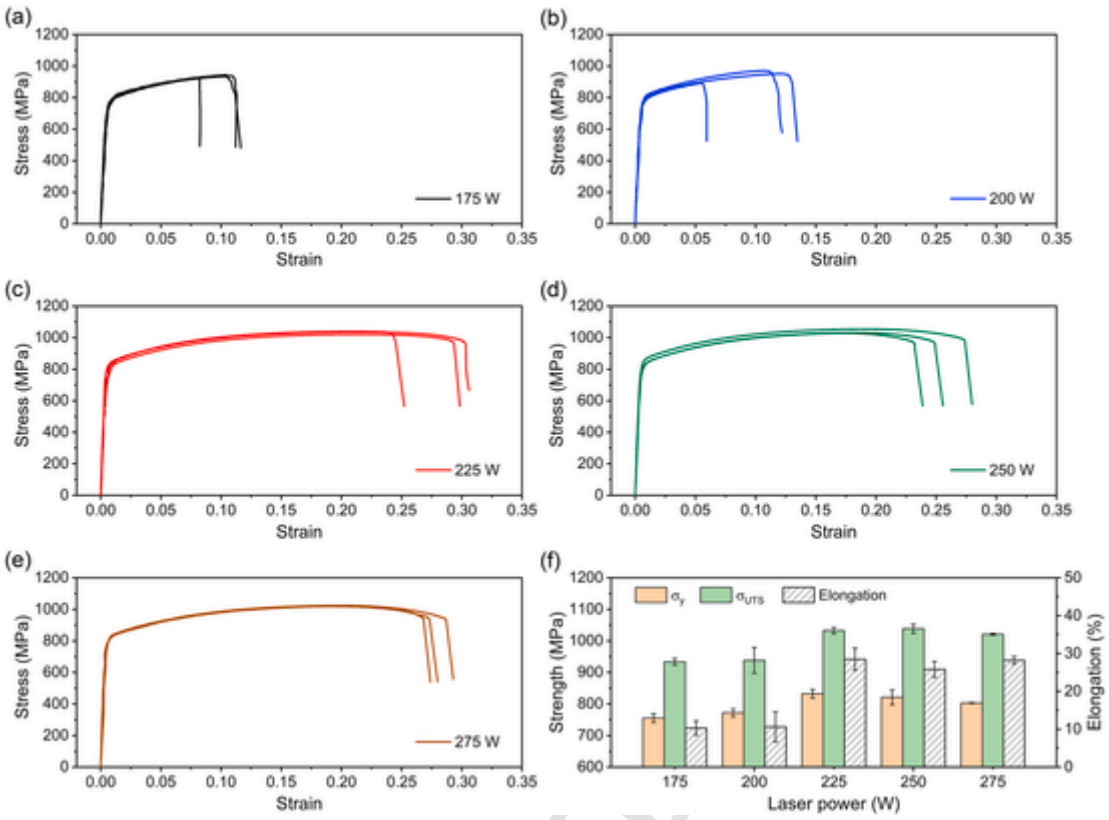

Fig. 12. The tensile stress-strain curves of SLM 316L-3TiC fabricated with the laser power of (a) 175 W, (b) 200 W, (c) 225 W, (d) 250 W and (e) 275 W. (f) A summary of the strength and elongation of the samples prepared with different laser powers.

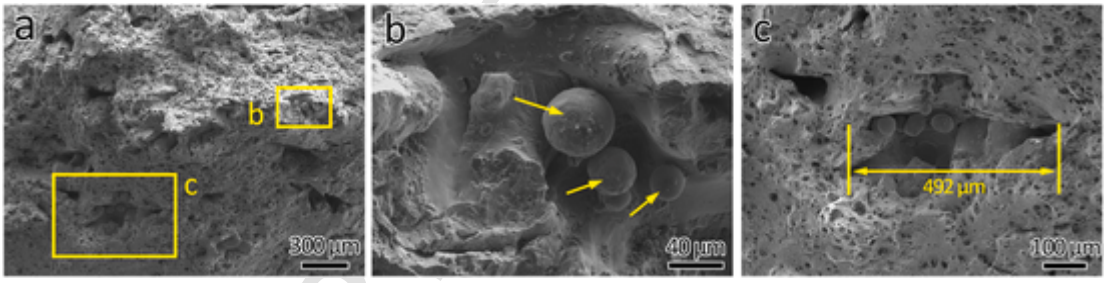

Fig. 13. SEM fractographs of SLM 316L-3TiC fabricated with the laser power of 175W showing the presence of unmelted 316L powders and cavities.

still much bigger than the TiC nanoparticles observed. All the experimental results indicate that the TiC nanoparticles were formed in-situ in the SLM processes.

A close-up of the in-situ formed TiC nanoparticles is shown in Fig. 15(b). It can be seen that the TiC nanoparticles are aligned at the cellular structure boundaries. TEM observation of the in-situ formed TiC nanoparticle is shown in Fig. 15(c). Fig. 15(d) shows the SAED pattern of γ-austenite phase from a [22–1] zone axis. Fig. 15(e) shows two sets of SAED patterns, i.e., austenite phase from a [22–1] zone axis and TiC nanosized phase from a [110] zone axis. The orientation relationship of austenite and TiC was derived from Fig. 15(e) is as follow: $(-110)_\gamma \parallel (1\text{–}11)_{TiC}$ $[22\text{–}1]_\gamma \parallel [110]_{TiC}$. Considering the parameters of $a_\gamma = 0.3591$ nm and $a_{TiC} = 0.4327$ nm, the corresponding interplanar spacings of $d_\gamma^{-110} = 0.254$ nm and $d_{TiC}^{1-11} = 0.250$ nm. Their mismatch of 1.6% shows that their interface is coherent.

The possible reason for the in-situ formation of TiC nanoparticles could be the micronsized TiC particles experienced partial melting during SLM. Simulation studies showed that the highest temperature of the melt pool exceeds 3000 K and that the temperature near the keyhole can reach 5000 K [31]. The temperature is well above the melting point of TiC, which is 3430 K. Therefore, it is reasonable to believe that micronsized TiC particles are partially melted during SLM process, especially given the observed unique shape of the TiC nanoparticle (Fig. 15 (c)) that is notably different from the original shape. The melted TiC presents as short-range orders within the melt. When the melt pool temperature falls to the melting point of TiC, TiC nanoparticles precipitate from the melt without coarsening because of the extremely high cooling rate (~10^7 K/s) of SLM. When the temperature of the melt pool decreases further to the melting point of 316L, the TiC nanoparticles can act as heterogeneous nucleation sites for austenite phase. After the melt pool is fully solidified, refined austenite grains are observed (Fig. 8).

A model is presented above to provide a plausible explanation for the in-situ formation of TiC nanoparticles observed. In this model, the micronsized TiC particles are assumed to be partially melted and dissolved without being decomposed. However, the possibility of TiC decomposition at high temperatures cannot be entirely excluded. If TiC would be decomposed into Ti and C at high temperatures, it would lead to solid solution of Ti and C in the 316L matrix and subsequent precipitation of TiC nanoparticles from the supersaturated solid solution at lower temperatures. The simple model presented needs to be studied

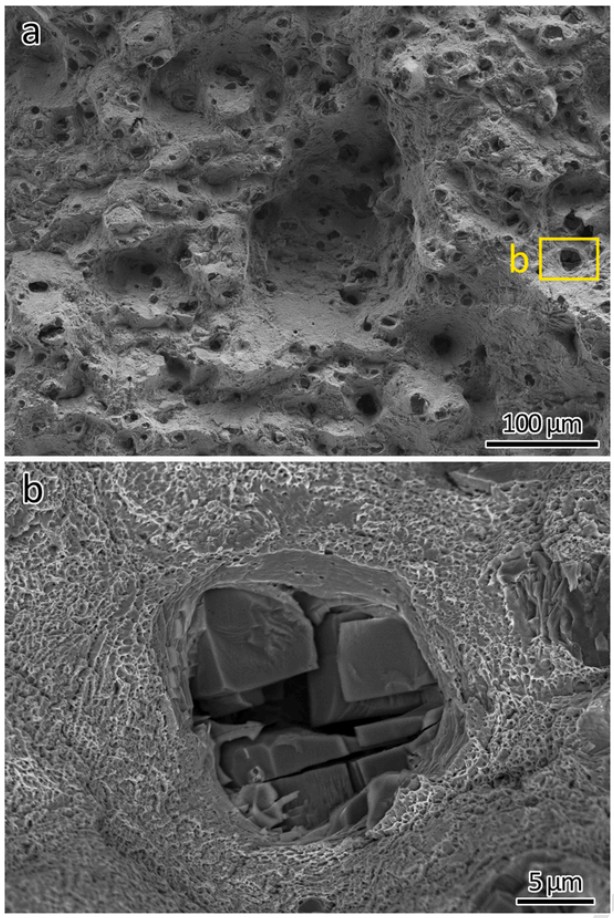

Fig. 14. (a) SEM fractographs of SLM 316L-3TiC fabricated with the laser power of 225 W showing no cavities; and (b) a close-up of a fractured TiC particle.

further to gain a better understanding of the in-situ formation mechanisms.

4.2. Strengthening mechanism

Compared with the 316L fabricated via SLM without TiC particles, the yield strength was increased from 599 MPa to 832 MPa [19]. The yield strength can be described using the Hall-Petch relationship,

$$\sigma_{H-P} = \sigma_o + \frac{K}{\sqrt{D}} \quad (1)$$

where σ_o is friction stress (MPa), K is Hall–Petch constant, and D is grain size (μm). An early study estimated that the Hall-Petch relationship for 316L is $\sigma_{H-P} = 181 + \frac{267}{\sqrt{D}}$ [7]. For the SLM 316L-3TiC, the average grain size measured using EBSD was 3.2 μm. Therefore, $\sigma_{H\_P} = 330$ MPa. For SLM 316L without the addition of TiC particles, the average grain size was 26 μm [19]. Therefore, for SLM 316L, $\sigma_{H-P} = 233$ MPa. Thus, the strength enhancement from grain refinement was calculated to be 97 MPa.

Orowan strengthening could be another contributor to SLM 316L-3TiC. Experimentally observed precipitation strengthening levels in micro-alloyed steels have shown excellent agreement with the prediction of the Ashby-Orowan equation [20],

$$\Delta\sigma_{Orowan} = \left(\frac{0.538Gb\sqrt{f}}{d}\right) ln\frac{d}{2b} \quad (2)$$

where $\Delta\sigma_{Orowan}$ is the increase in yield strength (MPa), G is shear modulus (MPa), b is Burgers vector (m), f is volume fraction of particles, and d is diameter of the particles (m). The in-situ formed TiC nanoparticles were observed using SEM (Fig. 15(a and b)) and TEM (Fig. 16(a)). Fig. 16(b) presents the size distribution of TiC, showing the average size measured at 62 nm and the volume fraction measured at 2.8%. The volume fraction of nanosized TiC particles indicates that about half of the micronsized TiC particles were transformed into nanosized particles. According to the Ashby-Orowan equation, G = 78 GPa, b = 0.258 nm [7], f = 2.8%, d = 62 nm. Therefore, $\Delta\sigma_{Orowan} = 140$ MPa.

Strain hardening from the high dislocation density (See Fig. 7(c)) generated due to rapid solidification under high thermal gradient in SLM is one of the significant contributors to the overall strength as well. The in-situ formed TiC nanoparticles additionally reduce the dislocation mean-free path, causing obstructions in the paths of gliding and even the formation of cells (low energy configuration), thereby forcing the dislocations to interact mutually. The flow stress during classical work-hardening usually varies in direct proportion with the square root of the dislocation density, according to the Taylor equation [32],

$$\Delta\sigma_d = AGb\sqrt{\rho} \quad (3)$$

where $\Delta\sigma_d$ is the increase in yield strength (MPa), A is 0.5 [33,34]. Assuming a dislocation density of 1.14×10^{15} m^{-2} typical for SLM process [35], we estimate $\Delta\sigma_d = 340$ MPa.

Overall, the total theoretical yield strength of SLM 316L-3TiC can be estimated by a summation of individual contributions (σ_{H-P}, $\Delta\sigma_{Orowan}$ and $\Delta\sigma_d$), which is 330 + 140 + 340 = 810 MPa. The experimentally observed yield strength of SLM 316L-3TiC is 803 - 832 MPa which is in reasonable agreement with the theoretical value.

Furthermore, it is noted from equation (1) that grain refinement can strengthen the yield strength. However, this would be dependent on the starting grain size and the level of grain refinement. Given a starting grain size of 316L of 100 μm, after grain refinement, the grain size is decreased by 85% to 15 μm, seemingly indicating significant grain refinement. However, the increase in strength is only 42.2 MPa, which is equivalent to 20.3% strengthening. On the other hand, considering a starting grain size of 16 μm, after grain refinement, the grain size would be decreased by 85% to 2.4 μm. The increase in strength will be 106.2 MPa, which is strengthened by 43%. The σ_{H-P} - grain size curve derived from the Hall-Petch relationship is shown in Fig. 17(a).

It is also noted from equation (2) that particle size has a much bigger effect on strengthening than volume fraction. If the volume fraction is increased by 4 times, the increase in strength would be doubled to 280 MPa. However, if the particle size is reduced from 62 nm to 6 nm, the increase in strength would be as high as 741 MPa. For instance, if micronsized particles of d = 6 μm were used, the increased strength would be only 3.5 MPa. This shows the significant contribution of nanoparticles to strengthening. The increase in yield strength – particle size curve derived from the Ashby-Orowan relationship is shown in Fig. 17(b). A sharp increase when the particle size is near 200 nm can be clearly observed resulting from the larger effect of particle size as discussed above.

The mechanical properties of 316L-3TiC in the current work surpassed all previous reports of particles strengthened 316L using laser additive manufacturing method, as shown in Table 1. Zhao et al. [18] added up to 4 wt% TiC nanoparticles into 316L. Unfortunately, the highest UTS of their 316L-TiC nanocomposite was only 748.6 MPa, with an elongation of only 24%. We added less micronsized TiC particles at only 3 wt%, but our results were significantly better in terms of both strength and ductility. Han et al. [36] reported that the addition of 0.1 wt% single-layer graphene nanoplatelets (GNPs) can also enhance the strength of 316L using SLM. The yield strength of 316L-GNP was 648 MPa with an elongation of 38%. Zhong et al. [37] reported the SLM of 316L with Y_2O_3 nanoparticles addition. However, only a small enhancement (4%) of yield strength was obtained (from 552 MPa to

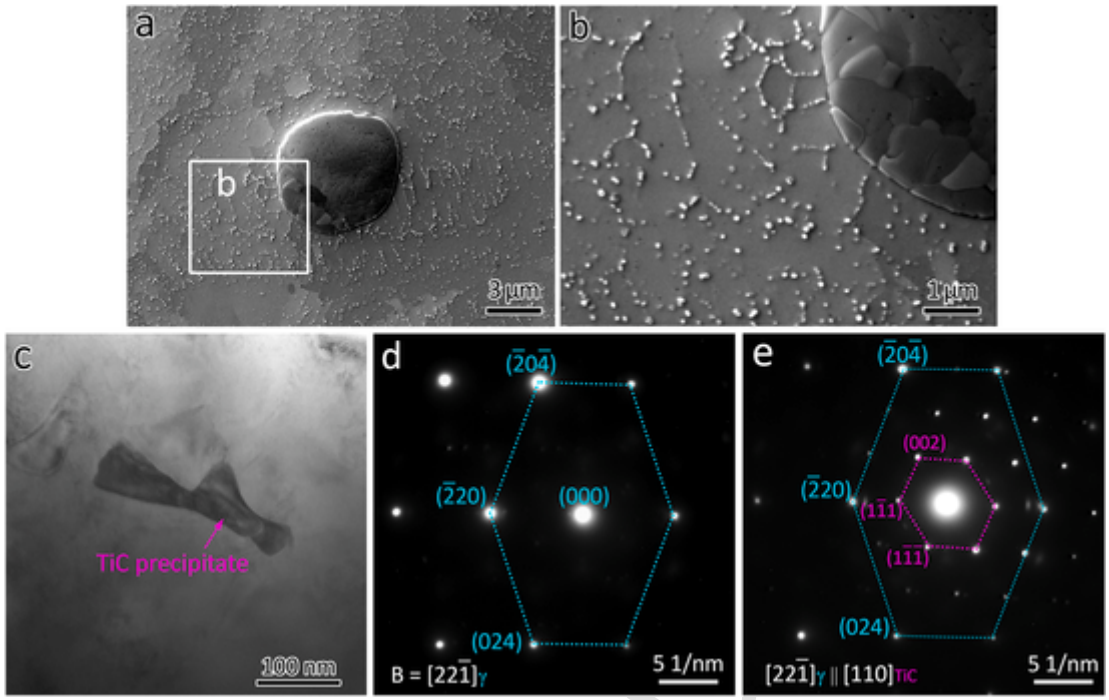

Fig. 15. In-situ formed TiC nanoprecipitates in 225 W sample. (a) SEM image showing the dispersion of the TiC nanoprecipitates; (b) a close-up of the TiC nanoprecipitates; (c) TEM bright-field image showing a region of interest consist of austenite matrix and a TiC nanoprecipitate, (d) SAED pattern of austenite phase, and (e) SAED patterns showing the orientation relationship.

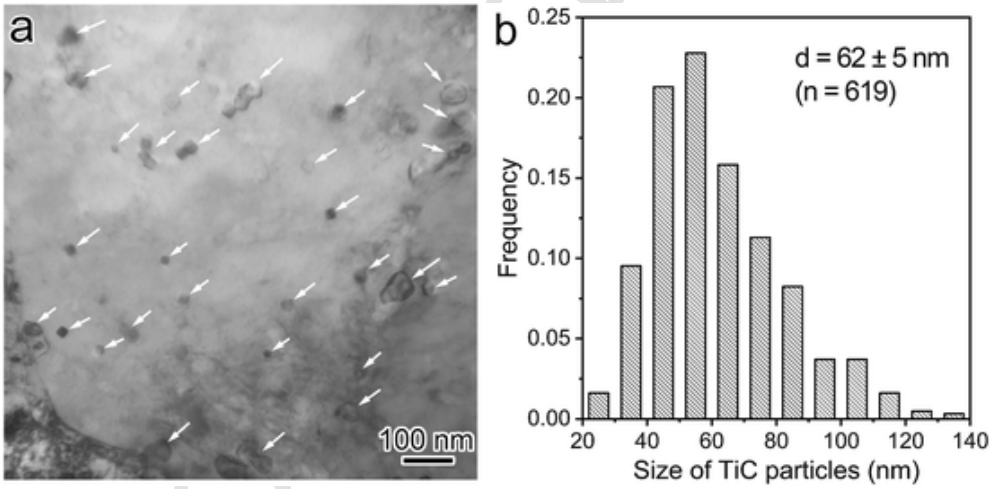

Fig. 16. (a) TEM bright-field image showing the in-situ formed TiC nanoparticles (pointed) from the 225 W sample and (b) their size distribution.

574 MPa) due to the agglomeration of the nanoparticles. Zou et al. [38] reported SiC strengthened 316L using SLM method. 316L-2.5SiC showed a high UTS at 1069 MPa but a poor elongation of about 7%. Wang et al. [39] reported TiN particles strengthened 316L fabricated using laser melting deposition process. The yield strength of 316L-2TiN is 323 MPa with an elongation of 30%. The strength is further enhanced to 394 and 457 MPa with 4 wt% and 6 wt% TiN addition. However, the elongation is reduced to a low level of 5%. As summarized above, the results in our work demonstrate the superior mechanical properties of SLM prepared TiC-strengthened 316L.

5. Conclusions

1. 316L-3TiC was fabricated with the laser power ranging from 150 to 275 W. Near full dense samples were fabricated with the laser powers of 225, 250 and 275 W. No cracks in the sample were observed when the highest laser power was applied, indicating a big processing window for the fabrication of 316L-3TiC via SLM;
2. In-situ formed nanosized TiC particles were observed, although micronsized TiC particles were added. The TiC nanoparticles are identified as precipitates. It was found that about 50% of the micronsized TiC particles were transformed into nanosized TiC particles with an average size of 62 nm, and were observed to be well dispersed in the matrix. Meanwhile, no intermetallic layer between TiC and the 316L matrix was formed;
3. High laser power induced a slightly larger grain size of 316L. The grain size was 2.7 μm with the laser power of 175 W and 3.5 μm with that of 275 W. The grain was significantly refined with the addition of micronsized TiC particles;
4. The experimentally observed yield strength of SLM 316L-3TiC was 803 MPa–832 MPa with the elongation ranging from 25.8% to 28.5% fabricated with the laser power between 225 and 275 W.

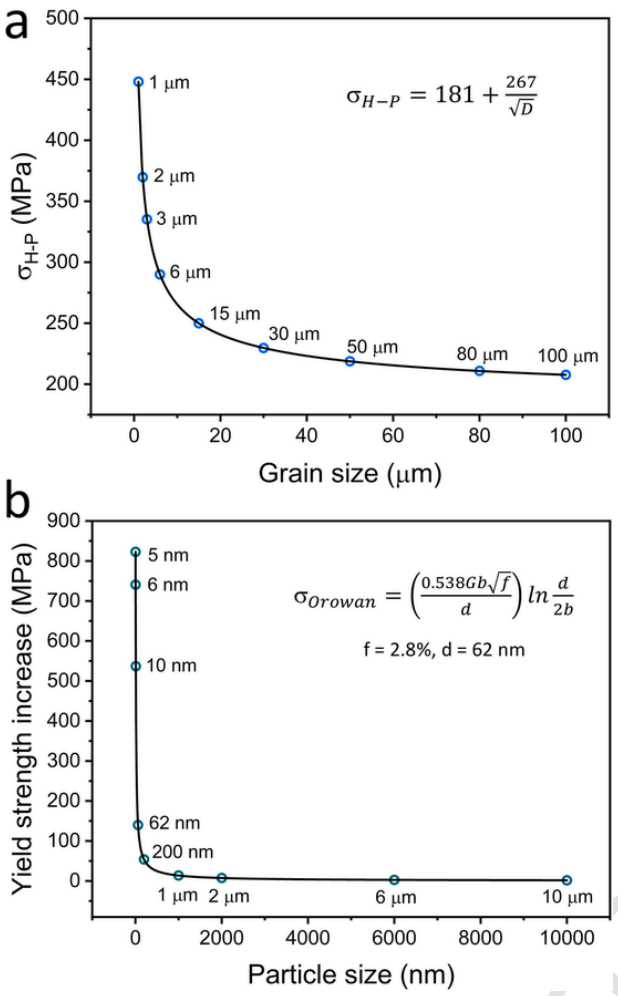

Fig. 17. (a) σ_{H-P} - grain size curve derived from the Hall-Petch relationship and (b) increase in yield strength - particle size curve derived from the Ashby-Orowan relationship.

Table 1
Comparison of mechanical properties of additively manufactured particles-strengthened 316L.

Material	Yield strength (MPa)	UTS (MPa)	Elongation (%)	Reference
316L-3TiC	832.3	1032.5	28.5	Current work
316L-2nanoTiC	–	748.6	24	[18]
316L-4nanoTiC	–	512.4	6.1	
316L-0.1GNP	648	738	38	[36]
316L-1Y_2O_3	574	–	90.5	[37]
316L-1.3SiC	–	786	12	[38]
316L-2.5SiC	–	1069	7	
316L-3.8SiC	–	1301	3	
316L-2TiN	323	640	30	[39]
316L-4TiN	394	533	5	
316L-6TiN	457	676	5	

Strength enhancement of 97 MPa from grain refinement and 140 MPa from Orowan strengthening was calculated.

CRediT authorship contribution statement

Wengang Zhai: Investigation, Validation, Formal analysis, Data curation, Visualization, Writing – original draft, Writing – review & editing, Conceptualization, Methodology, Writing – review & editing, Supervision. **Sharon Mui Ling Nai:** Resources, Writing – review & editing, Supervision.

Declaration of competing interest

The authors declare that they have no known competing financial interests or personal relationships that could have appeared to influence the work reported in this paper.

Acknowledgements

The authors acknowledge the support from A*STAR for access to Industrial Additive Manufacturing Facility (IAMF) and the support from Nanyang Technological University for access to the materials characterization facilities. We would like to acknowledge the Facility for Analysis, Characterisation, Testing and Simulation, Nanyang Technological University, Singapore, for use of their electron microscopy facilities.

References

[1] L. Liu, Q. Ding, Y. Zhong, J. Zou, J. Wu, Y.-L. Chiu, J. Li, Z. Zhang, Q. Yu, Z. Shen, Dislocation network in additive manufactured steel breaks strength–ductility trade-off, Mater. Today 21 (4) (2018) 354–361, https://doi.org/10.1016/j.mattod.2017.11.004.
[2] F.K. Yan, G.Z. Liu, N.R. Tao, K. Lu, Strength and ductility of 316L austenitic stainless steel strengthened by nano-scale twin bundles, Acta Mater. 60 (3) (2012) 1059–1071, https://doi.org/10.1016/j.actamat.2011.11.009.
[3] X.H. Chen, J. Lu, L. Lu, K. Lu, Tensile properties of a nanocrystalline 316L austenitic stainless steel, Scripta Mater. 52 (10) (2005) 1039–1044, https://doi.org/10.1016/j.scriptamat.2005.01.023.
[4] M. Eskandari, A. Najafizadeh, A. Kermanpur, Effect of strain-induced martensite on the formation of nanocrystalline 316L stainless steel after cold rolling and annealing, Mater. Sci. Eng. A 519 (1–2) (2009) 46–50, https://doi.org/10.1016/j.msea.2009.04.038.
[5] H. Ueno, K. Kakihata, Y. Kaneko, S. Hashimoto, A. Vinogradov, Enhanced fatigue properties of nanostructured austenitic SUS 316L stainless steel, Acta Mater. 59 (18) (2011) 7060–7069, https://doi.org/10.1016/j.actamat.2011.07.061.
[6] Y. Mine, Z. Horita, Y. Murakami, Effect of hydrogen on martensite formation in austenitic stainless steels in high-pressure torsion, Acta Mater. 57 (10) (2009) 2993–3002, https://doi.org/10.1016/j.actamat.2009.03.006.
[7] F.K. Yan, Q. Li, N.R. Tao, Anisotropic strengthening of nanotwinned austenitic grains in a nanotwinned stainless steel, Scripta Mater. 142 (2018) 15–19, https://doi.org/10.1016/j.scriptamat.2017.08.015.
[8] L. Lu, X. Chen, X. Huang, K. Lu, Revealing the maximum strength in nanotwinned copper, Science 323 (5914) (2009) 607–610, https://doi.org/10.1126/science.1167641.
[9] Y.M. Wang, T. Voisin, J.T. McKeown, J. Ye, N.P. Calta, Z. Li, Z. Zeng, Y. Zhang, W. Chen, T.T. Roehling, R.T. Ott, M.K. Santala, P.J. Depond, M.J. Matthews, A.V. Hamza, T. Zhu, Additively manufactured hierarchical stainless steels with high strength and ductility, Nat. Mater. 17 (1) (2018) 63–71, https://doi.org/10.1038/nmat5021.
[10] Z. Sun, X. Tan, S.B. Tor, C.K. Chua, Simultaneously enhanced strength and ductility for 3D-printed stainless steel 316L by selective laser melting, NPG Asia Mater. 10 (4) (2018) 127–136, https://doi.org/10.1038/s41427-018-0018-5.
[11] D. Kong, C. Dong, X. Ni, L. Zhang, J. Yao, C. Man, X. Cheng, K. Xiao, X. Li, Mechanical properties and corrosion behavior of selective laser melted 316L stainless steel after different heat treatment processes, J. Mater. Sci. Technol. 35 (7) (2019) 1499–1507, https://doi.org/10.1016/j.jmst.2019.03.003.
[12] M.L. Montero-Sistiaga, M. Godino-Martinez, K. Boschmans, J.-P. Kruth, J. Van Humbeeck, K. Vanmeensel, Microstructure evolution of 316L produced by HP-SLM (high power selective laser melting), Addit. Manuf. 23 (2018) 402–410, https://doi.org/10.1016/j.addma.2018.08.028.
[13] M. Kazemipour, M. Mohammadi, E. Mfoumou, A.M. Nasiri, Microstructure and corrosion characteristics of selective laser-melted 316L stainless steel: the impact of process-induced porosities, JOM (J. Occup. Med.) 71 (9) (2019) 3230–3240, https://doi.org/10.1007/s11837-019-03647-w.
[14] M.J.K. Lodhi, K.M. Deen, M.C. Greenlee-Wacker, W. Haider, Additively manufactured 316L stainless steel with improved corrosion resistance and biological response for biomedical applications, Addit. Manuf. 27 (2019) 8–19, https://doi.org/10.1016/j.addma.2019.02.005.
[15] B. AlMangour, D. Grzesiak, M. Jenn, Selective laser melting of TiC reinforced 316L stainless steel matrix nanocomposites: influence of starting TiC particle size and volume content, Mater. Des. 104 (2016) 141–151, https://doi.org/10.1016/j.matdes.2016.05.018.
[16] B. AlMangour, M.-S. Baek, D. Grzesiak, K.-A. Lee, Strengthening of stainless steel by titanium carbide addition and grain refinement during selective laser melting, Mater. Sci. Eng., A 712 (2018) 812–818, https://doi.org/10.1016/j.msea.2017.11.126.
[17] S. Dadbakhsh, R. Mertens, G. Ji, B. Vrancken, K. Vanmeensel, H. Fan, A. Addad, J.-P. Kruth, Heat treatment possibilities for an in situ βTi-TiC composite made by laser powder bed fusion, Addit. Manuf. 36 (2020) 101577, https://doi.org/10.1016/j.addma.2020.101577.
[18] S. Zhao, X. Shen, J. Yang, W. Teng, Y. Wang, Densification behavior and mechanical properties of nanocrystalline TiC reinforced 316L stainless steel

composite parts fabricated by selective laser melting, Opt. Laser. Technol. 103 (2018) 239–250, https://doi.org/10.1016/j.optlastec.2018.01.005.
[19] W. Zhai, Z. Zhu, W. Zhou, S.M.L. Nai, J. Wei, Selective laser melting of dispersed TiC particles strengthened 316L stainless steel, Compos. B Eng. 199 (2020) 108291, https://doi.org/10.1016/j.compositesb.2020.108291.
[20] T. Gladman, Precipitation hardening in metals, Mater. Sci. Technol. 15 (1) (1999) 30–36, https://doi.org/10.1179/026708399773002782.
[21] W. Zhai, W. Zhou, S.M.L. Nai, J. Wei, Characterization of nanoparticle mixed 316 L powder for additive manufacturing, J. Mater. Sci. Technol. 47 (2020) 162–168, https://doi.org/10.1016/j.jmst.2020.02.019.
[22] C. Hong, D. Gu, D. Dai, A. Gasser, A. Weisheit, I. Kelbassa, M. Zhong, R. Poprawe, Laser metal deposition of TiC/Inconel 718 composites with tailored interfacial microstructures, Opt. Laser. Technol. 54 (2013) 98–109, https://doi.org/10.1016/j.optlastec.2013.05.011.
[23] H. Chen, D. Gu, K. Kosiba, T. Lu, L. Deng, L. Xi, U. Kühn, Achieving high strength and high ductility in WC-reinforced iron-based composites by laser additive manufacturing, Addit. Manuf. 35 (2020) 101195, https://doi.org/10.1016/j.addma.2020.101195.
[24] M. Kiviö, L. Holappa, S. Louhenkilpi, M. Nakamoto, T. Tanaka, Studies on interfacial phenomena in titanium carbide/liquid steel systems for development of functionally graded, Metall. Mater. Trans. B 47 (4) (2016) 2114–2122, https://doi.org/10.1007/s11663-016-0658-1.
[25] S. Dryepondt, P. Nandwana, P. Fernandez-Zelaia, F. List, Microstructure and high temperature tensile properties of 316L fabricated by laser powder-bed fusion, Addit. Manuf. 37 (2021), https://doi.org/10.1016/j.addma.2020.101723.
[26] G. Wang, H. Ouyang, C. Fan, Q. Guo, Z. Li, W. Yan, Z. Li, The origin of high-density dislocations in additively manufactured metals, Mater. Res. Lett. 8 (8) (2020) 283–290, https://doi.org/10.1080/21663831.2020.1751739.
[27] T. Niendorf, S. Leuders, A. Riemer, H.A. Richard, T. Tröster, D. Schwarze, Highly anisotropic steel processed by selective laser melting, Metall. Mater. Trans. B 44 (4) (2013) 794–796, https://doi.org/10.1007/s11663-013-9875-z.
[28] M.J. Uddin, E. Ramirez-Cedillo, R.A. Mirshams, H.R. Siller, Nanoindentation and electron backscatter diffraction mapping in laser powder bed fusion of stainless steel 316L, Mater. Char. (2021) 174, https://doi.org/10.1016/j.matchar.2021.111047.
[29] O. Andreau, I. Koutiri, P. Peyre, J.-D. Penot, N. Saintier, E. Pessard, T. De Terris, C. Dupuy, T. Baudin, Texture control of 316L parts by modulation of the melt pool morphology in selective laser melting, J. Mater. Process. Technol. 264 (2019) 21–31, https://doi.org/10.1016/j.jmatprotec.2018.08.049.
[30] P. Wang, M.H. Goh, Q. Li, M.L.S. Nai, J. Wei, Effect of defects and specimen size with rectangular cross-section on the tensile properties of additively manufactured components, Virtual Phys. Prototyp. (2020) 1–14, https://doi.org/10.1080/17452759.2020.1733430.
[31] S.A. Khairallah, A. Anderson, Mesoscopic simulation model of selective laser melting of stainless steel powder, J. Mater. Process. Technol. 214 (11) (2014) 2627–2636, https://doi.org/10.1016/j.jmatprotec.2014.06.001.
[32] Z.G. Zhu, X.H. An, W.J. Lu, Z.M. Li, F.L. Ng, X.Z. Liao, U. Ramamurty, S.M.L. Nai, J. Wei, Selective laser melting enabling the hierarchically heterogeneous microstructure and excellent mechanical properties in an interstitial solute strengthened high entropy alloy, Mater. Res. Lett. 7 (11) (2019) 453–459, https://doi.org/10.1080/21663831.2019.1650131.
[33] H. Mecking, U.F. Kocks, Kinetics of flow and strain-hardening, Acta Metall. 29 (11) (1981) 1865–1875, https://doi.org/10.1016/0001-6160(81)90112-7.
[34] M.E. Kassner, A case for Taylor hardening during primary and steady-state creep in alurniniurn and type 304 stainless steel, J. Mater. Sci. 25 (1990) 1997–2003, https://doi.org/10.1007/BF01045755.
[35] Y.J. Yin, J.Q. Sun, J. Guo, X.F. Kan, D.C. Yang, Mechanism of high yield strength and yield ratio of 316 L stainless steel by additive manufacturing, Mater. Sci. Eng., A 744 (2019) 773–777, https://doi.org/10.1016/j.msea.2018.12.092.
[36] Y. Han, Y. Zhang, H. Jing, D. Lin, L. Zhao, L. Xu, P. Xin, Selective laser melting of low-content graphene nanoplatelets reinforced 316L austenitic stainless steel matrix: strength enhancement without affecting ductility, Addit. Manuf. 34 (2020) 101381, https://doi.org/10.1016/j.addma.2020.101381.
[37] Y. Zhong, L. Liu, J. Zou, X. Li, D. Cui, Z. Shen, Oxide dispersion strengthened stainless steel 316L with superior strength and ductility by selective laser melting, J. Mater. Sci. Technol. 42 (2020) 97–105, https://doi.org/10.1016/j.jmst.2019.11.004.
[38] Y. Zou, C. Tan, Z. Qiu, W. Ma, M. Kuang, D. Zeng, Additively manufactured SiC-reinforced stainless steel with excellent strength and wear resistance, Addit. Manuf. 41 (2021) 101971, https://doi.org/10.1016/j.addma.2021.101971.
[39] Y. Wang, Z. Liu, Y. Zhou, X. Yang, J. Tang, X. Liu, J. Li, G. Le, Microstructure and mechanical properties of TiN particles strengthened 316L steel prepared by laser melting deposition process, Mater. Sci. Eng., A 814 (2021) 141200, https://doi.org/10.1016/j.msea.2021.141220.